Acta Mech 227, 969–991 (2016)
DOI 10.1007/s00707-015-1503-3

ORIGINAL PAPER

G. Giunta · S. Belouettar · A. J. M. Ferreira

A static analysis of three-dimensional functionally graded beams by hierarchical modelling and a collocation meshless solution method

Received: 24 June 2015 / Revised: 13 October 2015 / Published online: 8 December 2015

Abstract In this paper, a mesh-free strong-form solution is used to investigate the static response of beams made of functionally graded materials. Thanks to a compact notation, the a priori expansion order of the three-dimensional displacement field upon the cross-section can be assumed as a free parameter resulting in a hierarchical kinematic modelling. Several higher-order theories as well as Timoshenko's classical model can be formulated straightforwardly. The governing differential equations and boundary conditions are obtained as a fundamental nucleus, and an algebraic system is derived via collocation with multiquadric radial basis functions. Results are validated towards three-dimensional FEM models and also against an analytical Navier-type solution. The numerical investigations demonstrate that the presented approach yields accurate results.

1 Introduction

The continuous and gradual change of mechanical and thermal properties along desired spatial directions makes functionally graded materials (FGMs) very attractive. The combination of different components with specific physical properties allows a tailored material design that broadens the structural design space leading to a multifunctional response with a minimal weight increase. Furthermore, beams play an important role in research since many primary and secondary structures such as aircraft wings, helicopter rotor blades or robot arms can be idealised by these structural elements. The static response of beam structures made of FGMs represents, therefore, an interesting and important research topic.

A brief overview of recent works about FGMs and the static analysis of FGM beams follows. An interesting historical overview on FGMs can be found in Koizumi [1]. A general account of FGMs (design, fabrication and applications) was presented by Suresh and Mortensen [2], Miyamoto et al. [3], Watanabe et al. [4] and Birman and Byrd [5]. As far as FGM beams modelling is concerned, Sankar [6] derived an exact elasticity solution for FGM beams with exponential Young's modulus and constant Poisson's ratio. An Euler–Bernoulli theory (EBT) was also derived where the shear stress component was obtained via integration of the indefinite equilibrium equations. Chakraborty et al. [7] developed a finite element based on Timoshenko's beam theory (TBT) for the static, free vibration and wave propagation analysis of FGM beams. The shape functions were derived from the general exact solution of the static governing equations. Mechanical and thermal material properties were

G. Giunta (✉) · S. Belouettar
Materials Research and Technology Department, Luxembourg Institute of Science and Technology,
5, avenue des Hauts-Fourneaux, 4362 Esch-sur-Alzette, Luxembourg
E-mail: gaetano.giunta@list.lu
Tel.: +352 54 55 80 479
Fax: +352 42 59 91 555

A. J. M. Ferreira
Departamento de Engenharia Mecânica e Gestão Industrial, Faculdade de Engenharia, Universidade do Porto,
Rua Dr. Roberto Frias, 4200-465 Porto, Portugal

assumed to vary along the thickness direction according to an exponential and a polynomial gradation law, respectively. Li [8] investigated the static and dynamic behaviour of FGM beams via a unified approach for classical EBT and TBT theories. Kapuria et al. [9] used a third-order zigzag theory for studying the static and free vibration response of layered FGM beams. The material gradation law was obtained via a modified rule of mixtures. Numerical investigations were validated by experimental results. Bîrsan et al. [10] used the direct approach proposed by Zhilin [11] for the analysis of composite and FGM beams where the stiffness elasticity tensors were obtained via comparison with three-dimensional elasticity static and free vibration solutions. The important contribution of Murin and co-workers [12–14] by the efficient and accurate modelling of FGM beam and shell elements should be, finally, mentioned.

As far as governing equation solution techniques are concerned, meshless methods were proposed over the past years to overcome several meshing-related problems. Liu and Gu [15] and Liu [16] presented a very comprehensive and thorough review on meshless methods. Computer implementation aspects were also addressed. Several meshless methods were discussed by showing their advantages and disadvantages and investigating different linear elasticity problems. The collocation method was also discussed. This latter is used in the present paper where multiquadric radial basis functions (RBFs) are adopted. Multiquadric RBFs were first proposed by Hardy [17] in topography for the analytical approximation of irregular surfaces using scattered data. Kansa [18,19] extended the approximation via RBFs first to estimate partial derivatives and, then, to the solution of partial differential equations (PDEs). Wu [20,21] provided a mathematical proof of the convergence of collocation with RBFs for both data interpolation and solution of PDEs: in the latter case, the order of convergence is $O(h^{d+1})$, being h the density of the collocation points and d a problem spatial dimension. Several structural problems have been solved by means of collocation with RBFs, see, for instance, Liu and Gu [22] and Liu and Wang [23]. To the best of the authors' knowledge, Ferreira [24,25] was amongst the first to study composite plate and beam structures by it. This solution method was successfully extended to FGM plates and shells in Roque et al. [26] and Neves et al. [27–31]. The advantages of collocation with RBFs reside in being easy to implement, providing higher-order smoothness of the solution and easiness in adding new collocation points to the solution space. Furthermore, since it is based on a strong-form solution, RBFs are evaluated only at nodes and not at the integration points, and they are differentiated but not integrated (this last task can be a problem in non-polynomial weak-form meshless methods). Finally, boundary conditions can easily be imposed. The loss of symmetry and sparsity (especially for globally supported RBFs) of the stiffness matrix should be mentioned as far as disadvantages are concerned. Some experience is required for the method to be used due to the presence of a shape parameter that has to be accurately chosen, and more details on this regard can be found in Davydov and Oanh [32].

A static analysis of three-dimensional FGM beams is addressed in this paper. The kinematic field is axiomatically assumed over the cross-section via a unified formulation (UF). This formulation was previously derived for plates and shells (see Carrera [33], Carrera and Giunta [34–36]) and then extended to the analysis of beam structures via finite element or Navier-type solutions, see Carrera and Giunta [37], Carrera et al. [38,39] and Giunta et al. [40–45]. The formulation is independent of the material gradation law in the sense that the variation of the material stiffness coefficients versus the cross-section coordinates is expressed by a bi-dimensional Lagrange approximation in terms of Newton's series expansion and Chebyshev points, see Philips [46]. The governing differential equations and the corresponding boundary conditions are derived from the principle of virtual displacement in terms of a fundamental nucleus that does not depend upon the displacement field approximation order. This latter can be assumed as a formulation free parameter. Displacement-based theories that account for non-classical effects, such as transverse shear and cross-section in- and out-of-plane warping, can be easily formulated. A strong-form meshless method based upon collocation with multiquadric RBFs is used to solve the derived governing equations and boundary conditions. Slender and deep beams are investigated. Cross-sections are made of an FGM mono-layer or present a sandwich configuration. A power law function is assumed for the material gradation. Simply supported boundary conditions are investigated. The proposed models are validated by comparison with three-dimensional FEM solutions. Closed-form Navier-type solutions based on the same kinematics here proposed are also presented. It should be noted that these latter solutions are exact within the theory approximation framework. Numerical results show that very accurate results can be obtained with a reduced computational effort when compared with traditional three-dimensional FEM solutions based upon solid elements.

2 Preliminaries

A beam is a structure whose axial extension (l) is predominant when compared with any other dimension orthogonal to it. The cross-section (Ω) is identified by intersecting the beam with planes that are orthogonal to its axis. A Cartesian reference system is adopted: y-axis and z-axis are two orthogonal directions laying on Ω. The x coordinate is coincident with the axis of the beam with $0 \leq x \leq l$. Beam geometry and reference system are shown in Fig. 1. The cross-section is considered to be constant along x. The displacement field is:

$$\mathbf{u}^{\mathrm{T}}(x, y, z) = \left\{ u_x(x, y, z) \quad u_y(x, y, z) \quad u_z(x, y, z) \right\} \tag{1}$$

in which u_x, u_y and u_z are the displacement components along x-, y- and z-axis, respectively. Superscript "T" represents the transposition operator. Stress, $\boldsymbol{\sigma}$, and strain, $\boldsymbol{\varepsilon}$, vectors are grouped into vectors $\boldsymbol{\sigma}_n$, $\boldsymbol{\varepsilon}_n$ that lay on the cross-section:

$$\boldsymbol{\sigma}_n^{\mathrm{T}} = \left\{ \sigma_{xx} \quad \sigma_{xy} \quad \sigma_{xz} \right\}, \quad \boldsymbol{\varepsilon}_n^{\mathrm{T}} = \left\{ \varepsilon_{xx} \quad \varepsilon_{xy} \quad \varepsilon_{xz} \right\} \tag{2}$$

and $\boldsymbol{\sigma}_p$, $\boldsymbol{\varepsilon}_p$ laying on planes orthogonal to Ω:

$$\boldsymbol{\sigma}_p^{\mathrm{T}} = \left\{ \sigma_{yy} \quad \sigma_{zz} \quad \sigma_{yz} \right\}, \quad \boldsymbol{\varepsilon}_p^{\mathrm{T}} = \left\{ \varepsilon_{yy} \quad \varepsilon_{zz} \quad \varepsilon_{yz} \right\}. \tag{3}$$

Under the hypothesis of linear analysis, the following strain–displacement geometrical relations hold:

$$\begin{aligned} \boldsymbol{\varepsilon}_n^{\mathrm{T}} &= \left\{ u_{x,x} \quad u_{x,y} + u_{y,x} \quad u_{x,z} + u_{z,x} \right\}, \\ \boldsymbol{\varepsilon}_p^{\mathrm{T}} &= \left\{ u_{y,y} \quad u_{z,z} \quad u_{y,z} + u_{z,y} \right\}. \end{aligned} \tag{4}$$

Subscripts "x", "y" and "z", when preceded by comma, represent derivation versus the corresponding spatial coordinate. A compact vectorial notation can be adopted for Eq. (4):

$$\begin{aligned} \boldsymbol{\varepsilon}_n &= \mathbf{D}_{np}\mathbf{u} + \mathbf{D}_{nx}\mathbf{u}, \\ \boldsymbol{\varepsilon}_p &= \mathbf{D}_p\mathbf{u} \end{aligned} \tag{5}$$

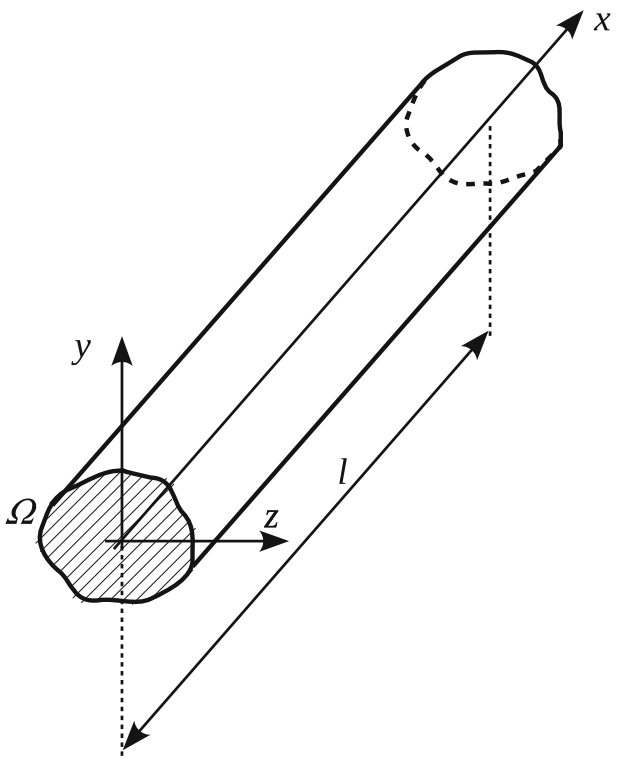

Fig. 1 Beam geometry and reference system

where $\mathbf{D}_{np}$, $\mathbf{D}_{nx}$ and $\mathbf{D}_p$ are the following differential matrix operators:

$$\mathbf{D}_{np} = \begin{bmatrix} 0 & 0 & 0 \\ \dfrac{\partial}{\partial y} & 0 & 0 \\ \dfrac{\partial}{\partial z} & 0 & 0 \end{bmatrix}, \quad \mathbf{D}_{nx} = \mathbf{I}\frac{\partial}{\partial x}, \quad \mathbf{D}_p = \begin{bmatrix} 0 & \dfrac{\partial}{\partial y} & 0 \\ 0 & 0 & \dfrac{\partial}{\partial z} \\ 0 & \dfrac{\partial}{\partial z} & \dfrac{\partial}{\partial y} \end{bmatrix}, \tag{6}$$

and $\mathbf{I}$ is the unit matrix. Under the hypothesis of linear elastic materials, the generalised Hooke's law holds. According to Eqs. (2) and (3), it reads:

$$\begin{aligned} \boldsymbol{\sigma}_p &= \mathbf{C}_{pp}\boldsymbol{\varepsilon}_p + \mathbf{C}_{pn}\boldsymbol{\varepsilon}_n, \\ \boldsymbol{\sigma}_n &= \mathbf{C}_{np}\boldsymbol{\varepsilon}_p + \mathbf{C}_{nn}\boldsymbol{\varepsilon}_n. \end{aligned} \tag{7}$$

In the case of isotropic FGMs, matrices $\mathbf{C}_{pp}$, $\mathbf{C}_{pn}$, $\mathbf{C}_{np}$ and $\mathbf{C}_{nn}$ in Eq. (7) are:

$$\mathbf{C}_{pp} = \begin{bmatrix} C_{11} & C_{12} & 0 \\ C_{12} & C_{11} & 0 \\ 0 & 0 & C_{44} \end{bmatrix}, \quad \mathbf{C}_{pn} = \mathbf{C}_{np}^{\mathrm{T}} = C_{12}\begin{bmatrix} 1 & 0 & 0 \\ 1 & 0 & 0 \\ 0 & 0 & 0 \end{bmatrix}, \quad \mathbf{C}_{nn} = \begin{bmatrix} C_{11} & 0 & 0 \\ 0 & C_{44} & 0 \\ 0 & 0 & C_{44} \end{bmatrix}. \tag{8}$$

The proposed models are implemented in a software tool in a very general manner that does not depend upon the particular gradation law. A Lagrange approximation on N_p Chebyshev points along y and z cross-section coordinates based on Newton series expansion is assumed for the material stiffness coefficients in Eq. (8):

$$C_{ij}(y,z) \approx \omega_\xi(y)\,\omega_\eta(z)\,C_{ij}\left[y_0,\ y_1,\ \ldots,\ y_\xi; z_0,\ z_1,\ \ldots,\ z_\eta\right] \ \text{ with } \ \xi,\eta = 0,\ 1,\ \ldots,\ N_p \tag{9}$$

being:

$$\omega_m(\zeta) = \begin{cases} 1 & m = 0 \\ \prod_{n=0}^{m-1}(\zeta - \zeta_n) & m \in \left[1, N_p\right] \end{cases}. \tag{10}$$

Chebyshev's points are defined on the domain $[-1, +1]$ via the following equation:

$$\zeta_m = \cos\left(\frac{m\pi}{N_p}\right) \ \text{ with } \ m = 0,\ 1,\ \ldots,\ N_p. \tag{11}$$

These points are, then, mapped into the cross-section domain via a variables transformation. Terms $C_{ij}[\ldots;\ldots]$ are the divided differences computed from the functions $C_{ij} = C_{ij}(y,z)$, see Philips [46]. These latter depend upon the particular gradation law chosen for the numerical investigations, or they can be obtained via numerical or analytical homogenisation analyses. In this article, a power gradation law of the volume fraction of the constituent metallic and ceramic materials and the rule of mixtures are assumed, see Praveen and Reddy [47] and Chakraborty et al. [7]. This results in a power law distribution over the cross-section of the Young's modulus E and the Poisson ratio ν:

$$\begin{aligned} E(y,z) &= (E_1 - E_2)\left(\alpha_y y + \beta_y\right)^{n_y}(\alpha_z z + \beta_z)^{n_z} + E_2, \\ \nu(y,z) &= (\nu_1 - \nu_2)\left(\alpha_y y + \beta_y\right)^{n_y}(\alpha_z z + \beta_z)^{n_z} + \nu_2 \end{aligned} \tag{12}$$

where α_y, α_z, β_y and β_z are defined according to the material reference system that can be different from the global structural one, and n_y and n_z are the material gradation exponents. The divided differences $C_{ij}[\ldots;\ldots]$ in Eq. (9) are then computed from:

$$\begin{aligned} C_{11}(y,z) &= \frac{1-\nu(y,z)}{[1+\nu(y,z)][1-2\nu(y,z)]}E(y,z), \\ C_{12}(y,z) &= \frac{\nu(y,z)}{[1+\nu(y,z)][1-2\nu(y,z)]}E(y,z), \\ C_{44}(y,z) &= \frac{1}{2[1+\nu(y,z)]}E(y,z), \end{aligned} \tag{13}$$

and Eq. (12). For the cases considered in the numerical investigations, nine Chebyshev's points along each cross-section axis ensure an accurate yet efficient approximation of the considered gradation law.

3 Hierarchical beam theories

The variation of the displacement field over the cross-section is postulated a priori. Several displacement-based theories can be formulated on the basis of the following generic kinematic field:

$$\mathbf{u}\,(x,\,y,\,z) = F_\tau\,(y,\,z)\,\mathbf{u}_\tau\,(x) \quad \text{with} \quad \tau = 1,\ 2,\ \ldots,\ N_\mathrm{u} \tag{14}$$

where N_u stands for the number of unknowns. It depends on the approximation order N which is a free parameter of the formulation. The compact expression is based on Einstein's notation: repeated indices implicitly indicate summation. Thanks to this notation, the problem's governing differential equations and boundary conditions can be derived in terms of a single fundamental nucleus. The complexity related to higher than classical approximation terms is tackled, and the theoretical formulation is valid for the generic approximation order and approximating functions $F_\tau\,(y,\,z)$. The approximating functions F_τ are Mac Laurin's polynomials. This choice is inspired by the classical beam models. N_u and F_τ as functions of N can be obtained by Pascal's triangle as shown in Table 1. The actual governing differential equations and boundary conditions due to a fixed approximation order are obtained straightforwardly via summation of the nucleus corresponding to each term of the expansion. According to the previous choice of polynomial function, the generic N-order displacement field is:

$$\begin{aligned}
u_x &= u_{x1} + u_{x2}y + u_{x3}z + \cdots + u_{x\frac{(N^2+N+2)}{2}}\,y^N + \cdots + u_{x\frac{(N+1)(N+2)}{2}}\,z^N,\\
u_y &= u_{y1} + u_{y2}y + u_{y3}z + \cdots + u_{y\frac{(N^2+N+2)}{2}}\,y^N + \cdots + u_{y\frac{(N+1)(N+2)}{2}}\,z^N,\\
u_z &= u_{z1} + u_{z2}y + u_{z3}z + \cdots + u_{z\frac{(N^2+N+2)}{2}}\,y^N + \cdots + u_{z\frac{(N+1)(N+2)}{2}}\,z^N.
\end{aligned} \tag{15}$$

The kinematic field of a first-order theory is:

$$\begin{aligned}
u_x &= u_{x1} + u_{x2}y + u_{x3}z,\\
u_y &= u_{y1} + u_{y2}y + u_{y3}z,\\
u_z &= u_{z1} + u_{z2}y + u_{z3}z.
\end{aligned} \tag{16}$$

TBT's displacement field:

$$\begin{aligned}
u_x &= u_{x1} + u_{x2}y + u_{x3}z,\\
u_y &= u_{y1},\\
u_z &= u_{z1}
\end{aligned} \tag{17}$$

is derived from the first-order approximation model. In this case, a reduced Hooke's law for the axial stress–strain relation should be used:

$$\sigma_{xx} = Q_{11}\varepsilon_{xx}. \tag{18}$$

This is due to the fact that the kinematic field in Eq. (17) accounts for a rigid cross-section ($\varepsilon_{yy} = \varepsilon_{zz} = 0$) in clear discordance with the Poisson effect:

$$\varepsilon_{ii} = -\nu\varepsilon_{xx} \neq 0 \quad \text{with} \quad i = y, z. \tag{19}$$

Table 1 Mac Laurin's polynomial terms via Pascal's triangle

N	N_u	F_τ
0	1	$F_1 = 1$
1	3	$F_2 = y\ \ F_3 = z$
2	6	$F_4 = y^2\ \ F_5 = yz\ \ F_6 = z^2$
3	10	$F_7 = y^3\ \ F_8 = y^2z\ \ F_9 = yz^2\ \ F_{10} = z^3$
...	...	...
N	$\frac{(N+1)(N+2)}{2}$	$F_{\frac{(N^2+N+2)}{2}} = y^N\ \ F_{\frac{(N^2+N+4)}{2}} = y^{N-1}z\ \ \ldots\ \ F_{\frac{N(N+3)}{2}} = yz^{N-1}\ \ F_{\frac{(N+1)(N+2)}{2}} = z^N$

This incongruence is known as Poisson's locking (see Carrera and Brischetto [48,49]), and it is tackled by using Eq. (18) instead of the full three-dimensional Hooke's equations in the normal stress components. The reduced material stiffness coefficient Q_{11} is classically obtained imposing the equations in σ_{yy} and σ_{zz} in Hooke's law equal to zero. An algebraic linear system in ε_{yy} and ε_{zz} is obtained, and by substituting its solution into Hooke's equations in σ_{xx}, the reduced stiffness coefficient Q_{11} is derived:

$$Q_{11} = C_{11} - 2C_{12}\frac{C_{12}^2 - C_{11}C_{12}}{C_{12}^2 - C_{11}^2}\,. \tag{20}$$

In the case of isotropic materials, Q_{11} is equal to Young's modulus E. In this last case, the reduced material stiffness law can be directly (and equivalently) obtained by replacing Eq. (19) within the Hooke's equations in the normal stress components. The equation in the axial stress results in Eq. (18) with $Q_{11} = E$, and the equations in the normal stresses ε_{yy} and ε_{zz} become the trivial identity. It should be noted that the shear stress–strain equations in Hooke's law are not reduced. In this work, no shear correction coefficient is considered, since it depends upon several parameters, such as the geometry of the cross-section (see, for instance, Cowper [50], Murty [51], Murin et al. [12]), and the main emphasis is posed on the higher-order models. Higher-order models yield a more detailed description of the shear mechanics, of the in- and out-of-section deformations, of the coupling of the spatial directions due to Poisson's effect and of the torsional mechanics than classical models do. A more general description of the proposed model as well as a detailed investigation of the effectiveness of each expansion term in the a priori kinematic field can be found in Carrera et al. [39] and Carrera and Petrolo [52].

4 Governing equations

The governing differential equations and the boundary conditions are obtained in terms of the displacement components by the principle of virtual displacements (PVD):

$$\delta L_i = \delta L_p \tag{21}$$

where L_i is the strain energy, L_p stands for the work due to external loadings, and δ represents a virtual variation.

4.1 Virtual variation of the strain energy

According to the grouping of the stress and strain components in Eqs. (2) and (3), the virtual variation of the strain energy is considered as the sum of two contributes:

$$\delta L_i = \int_l \int_\Omega \left(\delta \boldsymbol{\epsilon}_n^{\mathrm{T}} \boldsymbol{\sigma}_n + \delta \boldsymbol{\epsilon}_p^{\mathrm{T}} \boldsymbol{\sigma}_p \right) \mathrm{d}\Omega \mathrm{d}x. \tag{22}$$

By substitution of the geometrical relations, Eq. (5), the material constitutive equations, Eq. (7), and the unified hierarchical approximation of the displacements, Eq. (14), and after integration by parts, Eq. (22) reads:

$$\begin{aligned}
\delta L_i = \int_l \delta \mathbf{u}_\tau^{\mathrm{T}} \int_\Omega \Big[& - \mathbf{D}_{nx}^{\mathrm{T}} \mathbf{C}_{np} F_\tau \left(\mathbf{D}_p F_s \mathbf{I} \right) - \mathbf{D}_{nx}^{\mathrm{T}} \mathbf{C}_{nn} F_\tau \left(\mathbf{D}_{np} F_s \mathbf{I} \right) - \mathbf{D}_{nx}^{\mathrm{T}} \mathbf{C}_{nn} F_\tau F_s \mathbf{D}_{nx} \\
& + \left(\mathbf{D}_{np} F_\tau \mathbf{I} \right)^{\mathrm{T}} \mathbf{C}_{np} \left(\mathbf{D}_p F_s \mathbf{I} \right) + \left(\mathbf{D}_{np} F_\tau \mathbf{I} \right)^{\mathrm{T}} \mathbf{C}_{nn} \left(\mathbf{D}_{np} F_s \mathbf{I} \right) + \left(\mathbf{D}_{np} F_\tau \mathbf{I} \right)^{\mathrm{T}} \mathbf{C}_{nn} F_s \mathbf{D}_{nx} \\
& + \left(\mathbf{D}_p F_\tau \mathbf{I} \right)^{\mathrm{T}} \mathbf{C}_{pp} \left(\mathbf{D}_p F_s \mathbf{I} \right) + \left(\mathbf{D}_p F_\tau \mathbf{I} \right)^{\mathrm{T}} \mathbf{C}_{pn} \left(\mathbf{D}_{np} F_s \mathbf{I} \right) + \left(\mathbf{D}_p F_\tau \mathbf{I} \right)^{\mathrm{T}} \mathbf{C}_{pn} F_s \mathbf{D}_{nx} \Big] \\
& \times \mathrm{d}\Omega \mathbf{u}_s \, \mathrm{d}x + \delta \mathbf{u}_\tau^{\mathrm{T}} \int_\Omega F_\tau \left[\mathbf{C}_{np} \left(\mathbf{D}_p F_s \mathbf{I} \right) + \mathbf{C}_{nn} \left(\mathbf{D}_{np} F_s \mathbf{I} \right) + \mathbf{C}_{nn} F_s \mathbf{D}_{nx} \right] \mathrm{d}\Omega \mathbf{u}_s \Big|_{x=0}^{x=l}
\end{aligned} \tag{23}$$

where the differential matrix operator $\mathbf{D}_{nx}^{\mathrm{T}}$ operates on $\mathbf{u}_s$. In a compact vectorial form:

$$\delta L_i = \int_l \delta \mathbf{u}_\tau^{\mathrm{T}} \, \overline{\mathbf{K}}^{\tau s} \, \mathbf{u}_s \, \mathrm{d}x + \left[\delta \mathbf{u}_\tau^{\mathrm{T}} \, \overline{\mathbf{\Pi}}^{\tau s} \, \mathbf{u}_s \right]_{x=0}^{x=l}. \tag{24}$$

The components of the differential linear stiffness matrix $\overline{\mathbf{K}}^{\tau s}$ are:

$$\begin{aligned}
&\overline{K}_{xx}^{\tau s} = J_{\tau,ys,y}^{66} + J_{\tau,zs,z}^{55} - J_{\tau s}^{11} \frac{\partial^2}{\partial x^2} \quad \overline{K}_{xy}^{\tau s} = \left(J_{\tau,ys}^{66} - J_{\tau s,y}^{12} \right) \frac{\partial}{\partial x} \quad \overline{K}_{xz}^{\tau s} = \left(J_{\tau,zs}^{55} - J_{\tau s,z}^{13} \right) \frac{\partial}{\partial x}, \\
&\overline{K}_{yy}^{\tau s} = J_{\tau,ys,y}^{22} + J_{\tau,zs,z}^{44} - J_{\tau s}^{66} \frac{\partial^2}{\partial x^2} \quad \overline{K}_{yx}^{\tau s} = \left(J_{\tau,ys}^{12} - J_{\tau s,y}^{66} \right) \frac{\partial}{\partial x} \quad \overline{K}_{yz}^{\tau s} = J_{\tau,ys,z}^{23} + J_{\tau,zs,y}^{44}, \\
&\overline{K}_{zz}^{\tau s} = J_{\tau,ys,y}^{44} + J_{\tau,zs,z}^{33} - J_{\tau s}^{55} \frac{\partial^2}{\partial x^2} \quad \overline{K}_{zx}^{\tau s} = \left(J_{\tau,zs}^{13} - J_{\tau s,z}^{55} \right) \frac{\partial}{\partial x} \quad \overline{K}_{zy}^{\tau s} = J_{\tau,zs,y}^{23} + J_{\tau,ys,z}^{44},
\end{aligned} \tag{25}$$

The generic term $J_{\tau(,\phi)s(,\xi)}^{gh}$ is a cross-section moment:

$$J_{\tau(,\phi)s(,\xi)}^{gh} = \int_\Omega C_{gh} F_{\tau(,\phi)} F_{s(,\xi)} \, \mathrm{d}\Omega, \tag{26}$$

and it is obtained via Gauss' integration. As far as the boundary conditions are concerned, the components of $\overline{\mathbf{\Pi}}^{\tau s}$ are:

$$\begin{aligned}
&\overline{\Pi}_{xx}^{\tau s} = J_{\tau s}^{11} \frac{\partial}{\partial x} \quad \overline{\Pi}_{xy}^{\tau s} = J_{\tau s,y}^{12} \quad \overline{\Pi}_{xz}^{\tau s} = J_{\tau s,z}^{13}, \\
&\overline{\Pi}_{yy}^{\tau s} = J_{\tau s}^{66} \frac{\partial}{\partial x} \quad \overline{\Pi}_{yx}^{\tau s} = J_{\tau s,y}^{66} \quad \overline{\Pi}_{yz}^{\tau s} = 0, \\
&\overline{\Pi}_{zz}^{\tau s} = J_{\tau s}^{55} \frac{\partial}{\partial x} \quad \overline{\Pi}_{zx}^{\tau s} = J_{\tau s,z}^{55} \quad \overline{\Pi}_{zy}^{\tau s} = 0.
\end{aligned} \tag{27}$$

4.2 Virtual work of the external loadings

The external work is supposed to be due to following surface load components:

$$\begin{cases} p_{yx}, \; p_{yy}, \; p_{yz} & \forall (x,y,z) \in \left\{ x \in [0,l] \, ; \; y = \hat{y} \, ; \; z \in \left[\tilde{z}_1, \tilde{z}_2 \right] \right\} \\ p_{zx}, \; p_{zy}, \; p_{zz} & \forall (x,y,z) \in \left\{ x \in [0,l] \, ; \; y \in \left[\tilde{y}_1, \tilde{y}_2 \right] \, ; \; z = \hat{z} \right\} \end{cases}. \tag{28}$$

The first subscript accounts for the normal of the surface the loading is applied on, whereas the second one stands for the loading direction. The generic loading is applied on the cross-section interval $\left[(\tilde{\square})_1, (\tilde{\square})_2 \right]$ at location $(\hat{\square})$. The total external virtual work is:

$$\delta L_p = \delta L_{p_{zz}} + \delta L_{p_{zx}} + \delta L_{p_{zy}} + \delta L_{p_{yy}} + \delta L_{p_{yx}} + \delta L_{p_{yz}}. \tag{29}$$

Its explicit terms are:

$$\begin{aligned}
\left(\delta L_{p_{yx}}, \; \delta L_{p_{zx}} \right) &= \int_l \delta u_{x\tau} \left(p_{yx} E_\tau^{\hat{y}}, \; p_{zx} E_\tau^{\hat{z}} \right) \mathrm{d}x, \\
\left(\delta L_{p_{yy}}, \; \delta L_{p_{zy}} \right) &= \int_l \delta u_{y\tau} \left(p_{yy} E_\tau^{\hat{y}}, \; p_{zy} E_\tau^{\hat{z}} \right) \mathrm{d}x, \\
\left(\delta L_{p_{yz}}, \; \delta L_{p_{zz}} \right) &= \int_l \delta u_{z\tau} \left(p_{yz} E_\tau^{\hat{y}}, \; p_{zz} E_\tau^{\hat{z}} \right) \mathrm{d}x
\end{aligned} \tag{30}$$

where:

$$E_{\tau}^{\hat{z}} = \int_{\tilde{y}_1}^{\tilde{y}_2} F_{\tau}\left(y, \tilde{z}\right) \mathrm{d}y, \quad E_{\tau}^{\hat{y}} = \int_{\tilde{z}_1}^{\tilde{z}_2} F_{\tau}\left(\tilde{y}, z\right) \mathrm{d}z. \tag{31}$$

4.3 Governing equations' and boundary conditions' fundamental nuclei

The explicit form of the fundamental nucleus of the governing equations is:

$$\begin{aligned}
&\delta u_{x\tau} : -J_{\tau s}^{11} u_{xs,xx} + \left(J_{\tau,zs,z}^{55} + J_{\tau,ys,y}^{66}\right) u_{xs} + \left(J_{\tau,ys}^{66} - J_{\tau s,y}^{12}\right) u_{ys,x} + \left(J_{\tau,zs}^{55} - J_{\tau s,z}^{13}\right) u_{zs,x} \\
&\quad = p_{zx} E_{\tau}^{\hat{z}} + p_{yx} E_{\tau}^{\hat{y}}, \\
&\delta u_{y\tau} : \left(J_{\tau,ys}^{12} - J_{\tau s,y}^{66}\right) u_{xs,x} - J_{\tau s}^{66} u_{ys,xx} + \left(J_{\tau,ys,y}^{22} + J_{\tau,zs,z}^{44}\right) u_{ys} + \left(J_{\tau,ys,z}^{23} + J_{\tau,zs,y}^{44}\right) u_{zs} \\
&\quad = p_{yy} E_{\tau}^{\hat{y}} + p_{zy} E_{\tau}^{\hat{z}}, \\
&\delta u_{z\tau} : \left(J_{\tau,zs}^{13} - J_{\tau s,z}^{55}\right) u_{xs,x} + \left(J_{\tau,zs,y}^{23} + J_{\tau,ys,z}^{44}\right) u_{ys} - J_{\tau s}^{55} u_{zs,xx} + \left(J_{\tau,zs,z}^{33} + J_{\tau,ys,y}^{44}\right) u_{zs} \\
&\quad p_{zz} E_{\tau}^{\hat{z}} + p_{yz} E_{\tau}^{\hat{y}}.
\end{aligned} \tag{32}$$

The fundamental nuclei of Dirichlet's or Neumann's boundary conditions at $x/l = 0$ and 1 are, respectively:

$$\begin{aligned}
&\text{either } u_{x\tau} = \tilde{u}_{x\tau} \text{ or } J_{\tau s}^{11} u_{xs,x} + J_{\tau s,y}^{12} u_{ys} + J_{\tau s,z}^{13} u_{zs} = 0, \\
&\text{either } u_{y\tau} = \tilde{u}_{y\tau} \text{ or } J_{\tau s,y}^{66} u_{xs} + J_{\tau s}^{66} u_{ys,x} = 0, \\
&\text{either } u_{z\tau} = \tilde{u}_{z\tau} \text{ or } J_{\tau s,z}^{55} u_{xs} + J_{\tau s}^{55} u_{zs,x} = 0.
\end{aligned} \tag{33}$$

For a fixed approximation order, the nucleus has to be expanded versus the indices τ and s in order to obtain the governing equations and the boundary conditions of the desired model.

5 Collocation with radial basis functions

A set $\mathcal{D} \subset [0, l]$ of N_n distinct nodes x_i along the beam axis is considered:

$$\mathcal{D} = \mathcal{D}_{\mathrm{I}} \cup \mathcal{D}_{\mathrm{E}} = \{x_i : i = 2, 3, \ldots, N_n - 1\} \cup \left\{x_1/l = 0, x_{N_n}/l = 1\right\} \tag{34}$$

where $\mathcal{D}_{\mathrm{I}}$ and $\mathcal{D}_{\mathrm{E}}$ are two subsets containing the internal and the external nodes, respectively.

The axial variation of the displacement field and its derivatives are approximated via a linear combination of multiquadric RBFs $\phi_i\left(\|x - x_i, c\|\right)$:

$$\begin{aligned}
\mathbf{u}_{\tau}\left(x\right) &= \mathbf{U}_{\tau i} \phi_i\left(\|x - x_i, c\|\right), \\
\mathbf{u}_{\tau,x}\left(x\right) &= \mathbf{U}_{\tau i} \phi_{i,x}\left(\|x - x_i, c\|\right) \quad \text{with } i = 1, 2, \ldots, N_n, \\
\mathbf{u}_{\tau,xx}\left(x\right) &= \mathbf{U}_{\tau i} \phi_{i,xx}\left(\|x - x_i, c\|\right)
\end{aligned} \tag{35}$$

where $\mathbf{U}_{\tau i}$ are the unknown linear combination coefficients, and:

$$\phi_i\left(\|x - x_i, c\|\right) = \sqrt{(x - x_i)^2 + c^2} \tag{36}$$

being c a shape parameter, see Roque and Ferreira [53], that has to be opportunely chosen as discussed in Sect. 6.

5.1 Stiffness matrix algebraic fundamental nucleus

The algebraic fundamental nucleus of the governing equation is obtained by replacing Eq. (35) into Eq. (32) and computing them for an internal node $x_j \in \mathcal{D}_{\mathrm{I}}$:

$$
\begin{aligned}
&\left[\left(J^{55}_{\tau,zs,z}+J^{66}_{\tau,ys,y}\right)\phi_{ij}-J^{11}_{\tau s}\phi_{ij,xx}\right]U_{xsi}+\left(J^{66}_{\tau,ys}-J^{12}_{\tau s,y}\right)\phi_{ij,x}U_{ysi}+\left(J^{55}_{\tau,zs}-J^{13}_{\tau s,z}\right)\phi_{ij,x}U_{zsi}\\
&\quad=p_{zx}E^{\hat{z}}_{\tau}+p_{yx}E^{\hat{y}}_{\tau},\\
&\left(J^{12}_{\tau,ys}-J^{66}_{\tau s,y}\right)\phi_{ij,x}U_{xsi}+\left[\left(J^{22}_{\tau,ys,y}+J^{44}_{\tau,zs,z}\right)\phi_{ij}-J^{66}_{\tau s}\phi_{ij,xx}\right]U_{ysi}+\left(J^{23}_{\tau,ys,z}+J^{44}_{\tau,zs,y}\right)\phi_{ij}U_{zsi}\\
&\quad=p_{yy}E^{\hat{y}}_{\tau}+p_{zy}E^{\hat{z}}_{\tau},\\
&\left(J^{13}_{\tau,zs}-J^{55}_{\tau s,z}\right)\phi_{ij,x}U_{xsi}+\left(J^{23}_{\tau,zs,y}+J^{44}_{\tau,ys,z}\right)\phi_{ij}U_{ysi}+\left[\left(J^{33}_{\tau,zs,z}+J^{44}_{\tau,ys,y}\right)\phi_{ij}-J^{55}_{\tau s}\phi_{ij,xx}\right]U_{zsi}\\
&\quad=p_{zz}E^{\hat{z}}_{\tau}+p_{yz}E^{\hat{y}}_{\tau}
\end{aligned}
\tag{37}
$$

where, for the sake of brevity, the following notation has been introduced:

$$
\phi_{ij(,x)(,xx)}=\phi_{i(,x)(,xx)}\left(\|x_j-x_i,c\|\right). \tag{38}
$$

Equation (37) can be rewritten into the following compact matrix form:

$$
\mathbf{K}^{\tau sij}\mathbf{U}_{si}=\mathbf{P}_{\tau j}. \tag{39}
$$

For a fixed approximation order N, the nucleus in Eq. (39) has to be expanded versus the indices τ and s (kinematic approximation) and i and j (number of collocation points).

5.2 Boundary conditions algebraic fundamental nucleus

The boundary conditions are obtained replacing Eq. (35) with Eq. (33):

$$
\begin{aligned}
&\text{either } U_{x\tau i}\phi_{ij}=\tilde{u}_{x\tau} \text{ or } J^{11}_{\tau s}\phi_{ij,x}U_{xsi}+J^{12}_{\tau s,y}\phi_{ij}U_{ysi}+J^{13}_{\tau s,z}\phi_{ij}U_{zsi}=0,\\
&\text{either } U_{y\tau i}\phi_{ij}=\tilde{u}_{y\tau} \text{ or } J^{66}_{\tau s,y}\phi_{ij}U_{xsi}+J^{66}_{\tau s}\phi_{ij,x}U_{ysi}=0,\\
&\text{either } U_{z\tau i}\phi_{ij}=\tilde{u}_{z\tau} \text{ or } J^{55}_{\tau s,z}\phi_{ij}U_{xsi}+J^{55}_{\tau s}\phi_{ij,x}U_{zsi}=0
\end{aligned}
\tag{40}
$$

where $\phi_{ij,x}$ is computed at either x_1 or x_{N_n}. The compact matrix form of the boundary conditions algebraic fundamental nucleus is:

$$
\mathbf{\Pi}^{\tau sij}\mathbf{U}_{si}=\mathbf{B}_{\tau j}, \tag{41}
$$

Also, this nucleus has to be expanded versus the indices τ, s, i and j.

A clamped edge is obtained imposing a Dirichlet-type boundary condition for the three displacement components:

$$
U_{x\tau i}\phi_{ij}=0,\quad U_{y\tau i}\phi_{ij}=0,\quad U_{z\tau i}\phi_{ij}=0. \tag{42}
$$

A free edge is obtained by satisfying the following Neumann's boundary conditions:

$$
\begin{aligned}
J^{11}_{\tau s}\phi_{ij,x}U_{xsi}+J^{12}_{\tau s,y}\phi_{ij}U_{ysi}+J^{13}_{\tau s,z}\phi_{ij}U_{zsi}&=0,\\
J^{66}_{\tau s,y}\phi_{ij}U_{xsi}+J^{66}_{\tau s}\phi_{ij,x}U_{ysi}&=0,\\
J^{55}_{\tau s,z}\phi_{ij}U_{xsi}+J^{55}_{\tau s}\phi_{ij,x}U_{zsi}&=0.
\end{aligned}
\tag{43}
$$

A simply supported edge is obtained by considering Dirichlet's boundary conditions for the cross-section displacement components and a Neumann's boundary condition for the axial displacement:

$$
\begin{aligned}
U_{y\tau i}\phi_{ij}&=0,\\
U_{z\tau i}\phi_{ij}&=0,\\
J^{11}_{\tau s}\phi_{ij,x}U_{xsi}+J^{12}_{\tau s,y}\phi_{ij}U_{ysi}+J^{13}_{\tau s,z}\phi_{ij}U_{zsi}&=0.
\end{aligned}
\tag{44}
$$

5.3 Resulting algebraic system

An algebraic linear system in $\mathbf{U}_{si}$ is obtained by computing the nucleus in Eq. (39) for each node in $\mathcal{D}_{\mathrm{I}}$ and the boundary conditions nucleus in Eq. (41) for each node in $\mathcal{D}_{\mathrm{E}}$ and assembling them:

$$\begin{bmatrix} \mathbf{K}^{\tau s21} & \mathbf{K}^{\tau s22} & \dots & \mathbf{K}^{\tau s2(N_n-2)} & \mathbf{K}^{\tau s2(N_n-1)} & \mathbf{K}^{\tau s2N_n} \\ \mathbf{K}^{\tau s31} & \mathbf{K}^{\tau s32} & \dots & \mathbf{K}^{\tau s3(N_n-2)} & \mathbf{K}^{\tau s3(N_n-1)} & \mathbf{K}^{\tau s3N_n} \\ \vdots & \vdots & \ddots & \vdots & \vdots & \vdots \\ \mathbf{K}^{\tau s(N_n-1)1} & \mathbf{K}^{\tau s(N_n-1)2} & \dots & \mathbf{K}^{\tau s(N_n-1)(N_n-2)} & \mathbf{K}^{\tau s(N_n-1)(N_n-1)} & \mathbf{K}^{\tau s(N_n-1)N_n} \\ \mathbf{\Pi}^{\tau s11} & \mathbf{\Pi}^{\tau s12} & \dots & \mathbf{\Pi}^{\tau s1(N_n-2)} & \mathbf{\Pi}^{\tau s1(N_n-1)} & \mathbf{\Pi}^{\tau s1N_n} \\ \mathbf{\Pi}^{\tau sN_n1} & \mathbf{\Pi}^{\tau sN_n2} & \dots & \mathbf{\Pi}^{\tau sN_n(N_n-2)} & \mathbf{\Pi}^{\tau sN_n(N_n-1)} & \mathbf{\Pi}^{\tau sN_nN_n} \end{bmatrix} \begin{Bmatrix} \mathbf{U}_{s1} \\ \mathbf{U}_{s2} \\ \vdots \\ \mathbf{U}_{sN_n-2} \\ \mathbf{U}_{sN_n-1} \\ \mathbf{U}_{sN_n} \end{Bmatrix} = \begin{Bmatrix} \mathbf{P}_{\tau 2} \\ \mathbf{P}_{\tau 3} \\ \vdots \\ \mathbf{P}_{\tau N_n-1} \\ \mathbf{B}_{\tau 1} \\ \mathbf{B}_{\tau N_n} \end{Bmatrix}. \tag{45}$$

Hon and Shaback [54] showed that a general proof of non-singularity of a linear system obtained via collocation with RBFs is impossible. Nevertheless, on the basis of the numerical evidence and experience, they concluded that singular cases are rare and they have to be appositely constructed. Increasing the order of the problem, the coefficients matrix, which is a dense matrix, can become ill-conditioned. Kansa and Hon [55] proposed several techniques, such as domain decomposition, variable shape parameter and truncated multiquadric basis functions, to improve the conditioning of the coefficients matrix. In the present work, it has been found that, increasing the expansion order N, the problem can be severely ill-conditioned. Nevertheless, equilibration of the coefficients matrix via row and column scaling was sufficient to obtain a well-conditioned problem for each considered case.

6 Numerical results and discussion

FGM beams made of alumina and steel are considered. The mechanical properties of alumina are as follows: $E_1 = 3.9 \times 10^5$ MPa, $\nu_1 = 0.25$. In the case of steel, the following mechanical properties are used: $E_2 = 2.1 \times 10^5$ MPa, $\nu_2 = 0.31$. E and ν vary along the y-axis according to the power gradation law in Eq. (12) with $n_y = 0.5,\ 1$ and 2. The beam support is $[0, l] \times [0, a] \times [0, b]$. Square cross-section with $a = b = 1$ m is considered. The length-to-side ratio l/a is equal to 100 and 10. Slender and deep beams are, therefore, investigated. The following sinusoidal surface loading is considered:

$$p_{yy}(x) = P_{yy} \sin\left(\frac{\pi}{l}x\right) \quad \forall\,(x, y, z) \in \{x \in [0, l]\,;\ y = a;\ z \in [0, b]\} \tag{46}$$

with $P_{yy} = 1$ Pa. Convergence analysis is performed considering both a uniform and a Chebyshev node distribution. This latter yields, for the considered cases, a faster convergence, and it will be adopted in the remaining of the numerical investigations. Results are put into the following dimensionless form:

$$\begin{aligned} \left(\overline{u}_y, \overline{u}_z\right) &= \frac{1}{a}\left(u_y, u_z\right), \\ \left(\overline{\sigma}_{xx}, \overline{\sigma}_{xy}, \overline{\sigma}_{yy}\right) &= \frac{1}{P_{yy}}\left(\sigma_{xx}, \sigma_{xy}, \sigma_{yy}\right). \end{aligned} \tag{47}$$

Simply supported beams are considered. Results are, then, thoroughly validated towards a closed-form Navier-type analytical solution using the same kinematics, see Giunta et al. [40]. Within the proposed beam

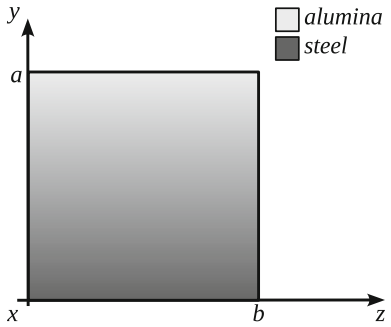

Fig. 2 Mono-layer beam cross-section

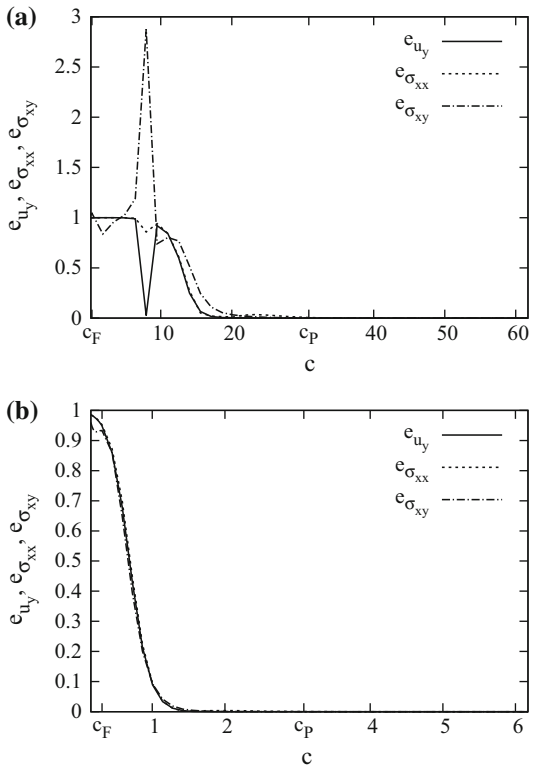

Fig. 3 Effect of the shape parameter c on the normalised difference between the RBF solution and the corresponding Navier-type solution for $N = 2,\ N_n = 21$ and **a** $l/a = 100$ and **b** ten, Chebyshev collocation points distribution

theory approximation, this latter represents an exact solution of the governing differential problem presented in Eqs. (32) and (33). Unless otherwise specified, the transverse displacement $\overline{u}_y$ is computed at $(l/2, a/2, b/2)$ and $\overline{u}_z$ at $(l/2, a, 0)$. Stress components $\overline{\sigma}_{xx}$ and $\overline{\sigma}_{xy}$ are evaluated at $(l/2, a, b/2)$ and $(0, a/2, b/2)$, respectively. Three-dimensional FEM solutions obtained via the commercial code ANSYS are also considered. The three-dimensional quadratic element "Solid186" is used, see ANSYS theory manual [56]. Each element is considered as homogeneous by referring to the material properties at its centre point. The accuracy of the three-dimensional FEM solution depends upon both the FEM numerical approximation and the approximation of the gradation law. A coarse and a fine mesh are considered in order to investigate the convergence of the reference solution. Thanks to the problem symmetry, only the $[0, l/2] \times [0, a] \times [0, b/2]$ quarter model is considered in the three-dimensional FEM problem. Although the three-dimensional FEM solution and the meshless one are different in nature, some considerations about computational effort can be addressed. The three-dimensional FEM models degrees of freedom (DOF) range between about 7×10^5 and 1.1×10^6. The number of DOF (N_{DOF}) for the present meshless method is a function of the expansion order N and the number of nodes N_n:

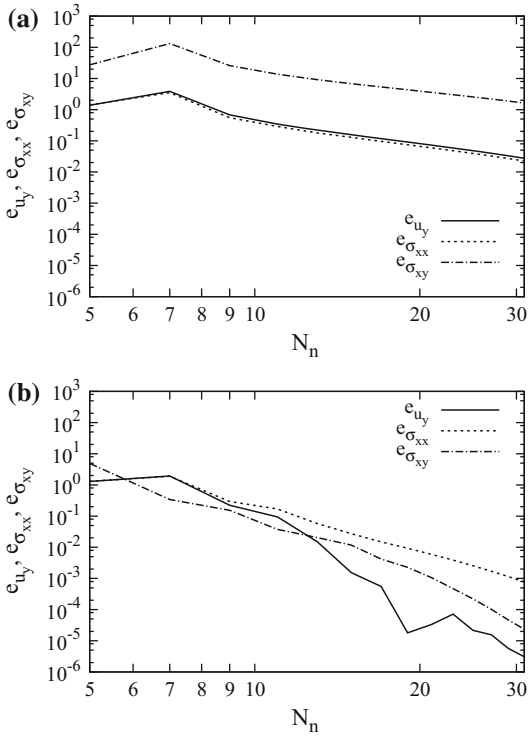

Fig. 4 Effect of the nodes number N_n on e_{u_y}, $e_{\sigma_{xx}}$ and $e_{\sigma_{xy}}$ for $l/a = 100$, $N = 2$ and $c = c_{\mathrm{P}}$ via **a** uniform and **b** Chebyshev collocation points distribution

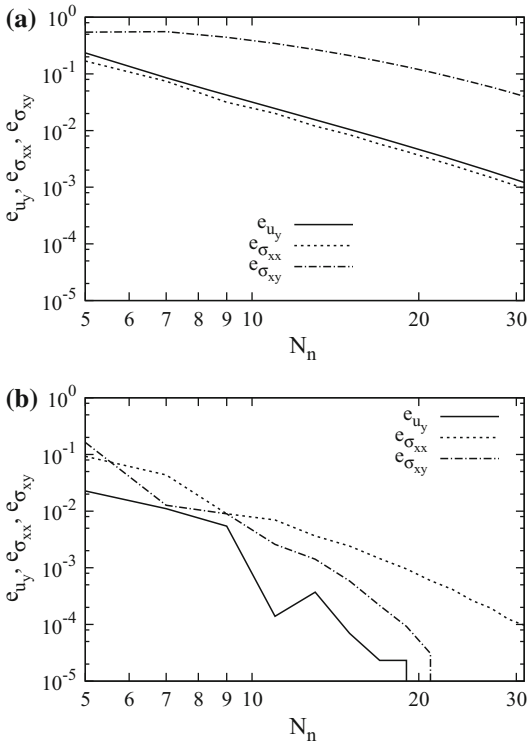

Fig. 5 Effect of the nodes number N_n on e_{u_y}, $e_{\sigma_{xx}}$ and $e_{\sigma_{xy}}$ for $l/a = 10$, $N = 2$ and $c = c_{\mathrm{P}}$ via **a** uniform and **b** Chebyshev collocation points distribution

Table 2 Dimensionless transverse displacement, mono-layer beam, $l/a = 100$

	$\overline{u}_y \times 10^5$		
	$n_y = 0.5$	$n_y = 1$	$n_y = 2$
FEM 3D[a]	3.873	4.234	4.530
FEM 3D[b]	3.869	4.232	4.531
Navier $N = 9$	3.881	4.234	4.530
$N = 9$	3.880	4.234	4.530
$N = 7$	3.881	4.234	4.530
$N = 6$	3.881	4.234	4.530
$N = 5$	3.881	4.234	4.530
$N = 4$	3.881	4.234	4.530
$N = 3$	3.880	4.234	4.529
$N = 2$	3.878	4.231	4.526
TBT	3.881	4.234	4.530

[a] Elements' number $60 \times 40 \times 20$
[b] Elements' number $30 \times 20 \times 10$

Table 3 Dimensionless displacements $\overline{u}_y$ and $\overline{u}_z$, mono-layer beam, $l/a = 10$

	$n_y = 0.5$		$n_y = 1$		$n_y = 2$	
	$\overline{u}_y \times 10^9$	$\overline{u}_z \times 10^{11}$	$\overline{u}_y \times 10^9$	$\overline{u}_z \times 10^{11}$	$\overline{u}_y \times 10^9$	$\overline{u}_z \times 10^{11}$
FEM 3D[a]	3.954	2.289	4.325	2.451	4.637	2.625
FEM 3D[b]	3.948	2.286	4.322	2.452	4.635	2.628
Navier $N = 9$	3.962	2.291	4.326	2.451	4.637	2.624
$N = 9$	3.963	2.291	4.326	2.451	4.637	2.624
$N = 7$	3.962	2.290	4.326	2.451	4.637	2.625
$N = 6$	3.962	2.296	4.326	2.455	4.637	2.629
$N = 5$	3.962	2.290	4.326	2.455	4.637	2.636
$N = 4$	3.962	2.296	4.326	2.460	4.637	2.640
$N = 3$	3.962	2.283	4.326	2.455	4.636	2.650
$N = 2$	3.948	2.373	4.309	2.567	4.616	2.767
TBT	3.958	0.000	4.320	0.000	4.626	0.000

[a] Elements' number $35 \times 40 \times 20$
[b] Elements' number $15 \times 20 \times 10$

Table 4 Dimensionless normal and shear stresses, mono-layer beam, $l/a = 100$

	$n_y = 0.5$		$n_y = 1$		$n_y = 2$	
	$\overline{\sigma}_{xx} \times 10^{-3}$	$\overline{\sigma}_{xy} \times 10^{-1}$	$\overline{\sigma}_{xx} \times 10^{-3}$	$\overline{\sigma}_{xy} \times 10^{-1}$	$\overline{\sigma}_{xx} \times 10^{-3}$	$\overline{\sigma}_{xy} \times 10^{-1}$
FEM 3D[a]	6.879	4.497	7.268	4.457	7.627	4.398
FEM 3D[b]	6.855	4.501	7.227	4.461	7.547	4.402
Navier $N = 9$	6.908	4.497	7.308	4.455	7.712	4.395
$N = 9$	6.904	4.636	7.306	4.442	7.709	4.355
$N = 7$	6.907	4.504	7.306	4.457	7.706	4.398
$N = 6$	6.902	4.504	7.304	4.451	7.705	4.394
$N = 5$	6.906	4.503	7.305	4.452	7.712	4.393
$N = 4$	6.908	4.530	7.321	4.488	7.729	4.400
$N = 3$	6.930	4.524	7.323	4.475	7.700	4.380
$N = 2$	6.834	3.288	7.203	3.245	7.576	3.076
TBT	6.920	3.256	7.330	3.175	7.745	2.986

[a] Elements' number $60 \times 40 \times 20$
[b] Elements' number $30 \times 20 \times 10$

$$N_{\mathrm{DOF}} = 3\frac{(N+1)\,(N+2)}{2} N_n. \tag{48}$$

In the case of a twelfth-order 21-node meshless solution (the highest considered one), it is equal to about 5.8×10^3. It should be noted that an analogous (as many nodes as the collocation points) solution by means of the finite element method in the framework of the proposed hierarchical beam modelling has the same number

Table 5 Dimensionless normal and shear stresses, mono-layer beam, $l/a = 10$

	$n_y = 0.5$		$n_y = 1$		$n_y = 2$	
	$\overline{\sigma}_{xx} \times 10^{-1}$	$\overline{\sigma}_{xy}$	$\overline{\sigma}_{xx} \times 10^{-1}$	$\overline{\sigma}_{xy}$	$\overline{\sigma}_{xx} \times 10^{-1}$	$\overline{\sigma}_{xy}$
FEM 3D[a]	6.908	4.493	7.301	4.453	7.664	4.394
FEM 3D[b]	6.884	4.497	7.260	4.458	7.584	4.398
Navier $N = 9$	6.937	4.493	7.341	4.451	7.748	4.391
$N = 9$	6.925	4.617	7.341	4.451	7.748	4.391
$N = 7$	6.938	4.500	7.341	4.454	7.745	4.394
$N = 6$	6.934	4.500	7.340	4.447	7.744	4.390
$N = 5$	6.937	4.499	7.339	4.448	7.750	4.389
$N = 4$	6.941	4.527	7.358	4.485	7.770	4.397
$N = 3$	6.972	4.520	7.369	4.471	7.752	4.376
$N = 2$	6.845	3.283	7.219	3.241	7.594	3.072
TBT	6.922	3.256	7.333	3.175	7.748	2.986

[a] Elements' number $35 \times 40 \times 20$
[b] Elements' number $15 \times 20 \times 10$

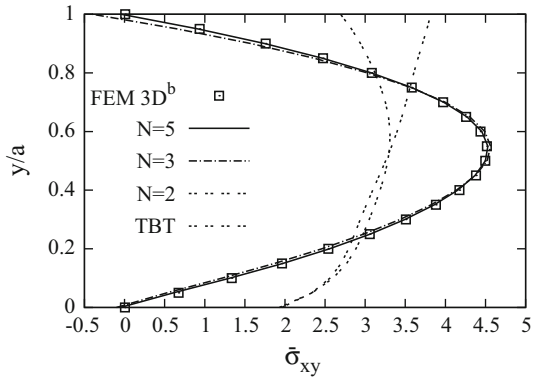

Fig. 6 Transverse shear stress $\overline{\sigma}_{xy}$ at $x = 0$ and $z = b/2$ along the y-axis in a mono-layer beam with $l/a = 10$ and $n_y = 0.5$

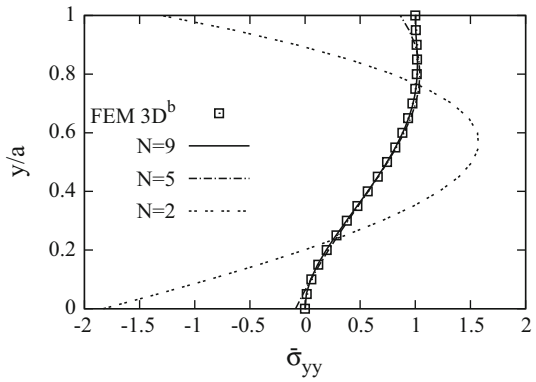

Fig. 7 Transverse normal stress $\overline{\sigma}_{yy}$ at $x = l/2$ and $z = b/2$ along the y-axis in a mono-layer beam with $l/a = 10$ and $n_y = 1$

of DOF. This latter solution has the advantage of yielding sparse matrices, whereas the one used in this paper results in smooth stresses. Nevertheless, the sparsity of the resulting stiffness matrix can be improved by means of locally supported radial basis functions such as Wendland's ones.

6.1 Mono-layer beams

A mono-layer alumina–steel FGM beam is considered. The material is fully metallic at $y = 0$ and fully ceramic at $y = a$ as shown in Fig. 2.

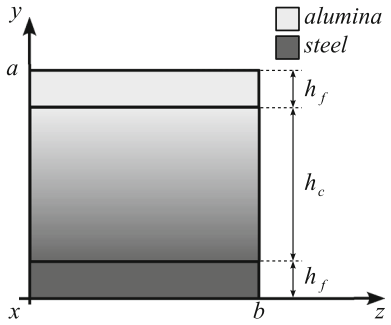

Fig. 8 Sandwich beam cross-section

Table 6 Dimensionless displacements $\overline{u}_y$ and $\overline{u}_z$, sandwich beam and $l/a = 10$

	$n_y = 0.5$		$n_y = 1$		$n_y = 2$	
	$\overline{u}_y \times 10^9$	$\overline{u}_z \times 10^{11}$	$\overline{u}_y \times 10^9$	$\overline{u}_z \times 10^{11}$	$\overline{u}_y \times 10^9$	$\overline{u}_z \times 10^{11}$
FEM 3D[a]	4.151	2.332	4.378	2.410	4.552	2.481
FEM 3D[b]	4.144	2.329	4.373	2.408	4.549	2.480
Navier $N = 9$	4.157	2.335	4.379	2.410	4.552	2.479
$N = 9$	4.157	2.336	4.379	2.411	4.552	2.480
$N = 8$	4.157	2.334	4.379	2.410	4.552	2.479
$N = 7$	4.156	2.334	4.379	2.409	4.552	2.478
$N = 6$	4.156	2.337	4.379	2.410	4.552	2.480
$N = 5$	4.156	2.330	4.379	2.411	4.552	2.485
$N = 4$	4.156	2.337	4.378	2.414	4.552	2.488
$N = 3$	4.156	2.317	4.378	2.408	4.551	2.496
$N = 2$	4.141	2.438	4.361	2.534	4.530	2.620
TBT	4.153	0.000	4.372	0.000	4.539	0.000

[a] Elements' number $35 \times 40 \times 20$
[a] Elements' number $15 \times 20 \times 10$

Table 7 Dimensionless normal and shear stresses, sandwich beam and $l/a = 10$

	$n_y = 0.5$		$n_y = 1$		$n_y = 2$	
	$\overline{\sigma}_{xx} \times 10^{-1}$	$\overline{\sigma}_{xy}$	$\overline{\sigma}_{xx} \times 10^{-1}$	$\overline{\sigma}_{xy}$	$\overline{\sigma}_{xx} \times 10^{-1}$	$\overline{\sigma}_{xy}$
FEM 3D[a]	7.085	4.512	7.291	4.447	7.476	4.385
FEM 3D[b]	7.082	4.516	7.291	4.451	7.478	4.388
Navier $N = 9$	7.088	4.515	7.289	4.445	7.471	4.380
$N = 9$	7.093	4.515	7.294	4.445	7.476	4.380
$N = 8$	7.099	4.536	7.295	4.447	7.477	4.386
$N = 7$	7.091	4.531	7.295	4.447	7.476	4.386
$N = 6$	7.102	4.502	7.298	4.437	7.478	4.385
$N = 5$	7.092	4.503	7.296	4.440	7.493	4.384
$N = 4$	7.109	4.527	7.329	4.488	7.525	4.373
$N = 3$	7.151	4.524	7.340	4.466	7.509	4.337
$N = 2$	6.992	3.370	7.176	3.269	7.343	3.030
TBT	7.079	3.317	7.279	3.172	7.462	2.913

[a] Elements' number $35 \times 40 \times 20$
[b] Elements' number $15 \times 20 \times 10$

6.1.1 Influence of the shape parameter

The influence of the shape parameter c is investigated first. It plays an important role in the accuracy of the collocation with RBFs for approximating functions (see Press et al. [57]) or solving partial differential equations (see Roque and Ferreira [53]). Accuracy can differ by several orders of magnitude according to a good or a poor choice of c. In general, the shape parameter should be larger than the average distance between two consecutive nodes and smaller than the problem leading dimension. In the literature, several values of c were proposed depending upon the number of nodes or the distance between the nodes or both. For instance, Fasshauer [58] suggested:

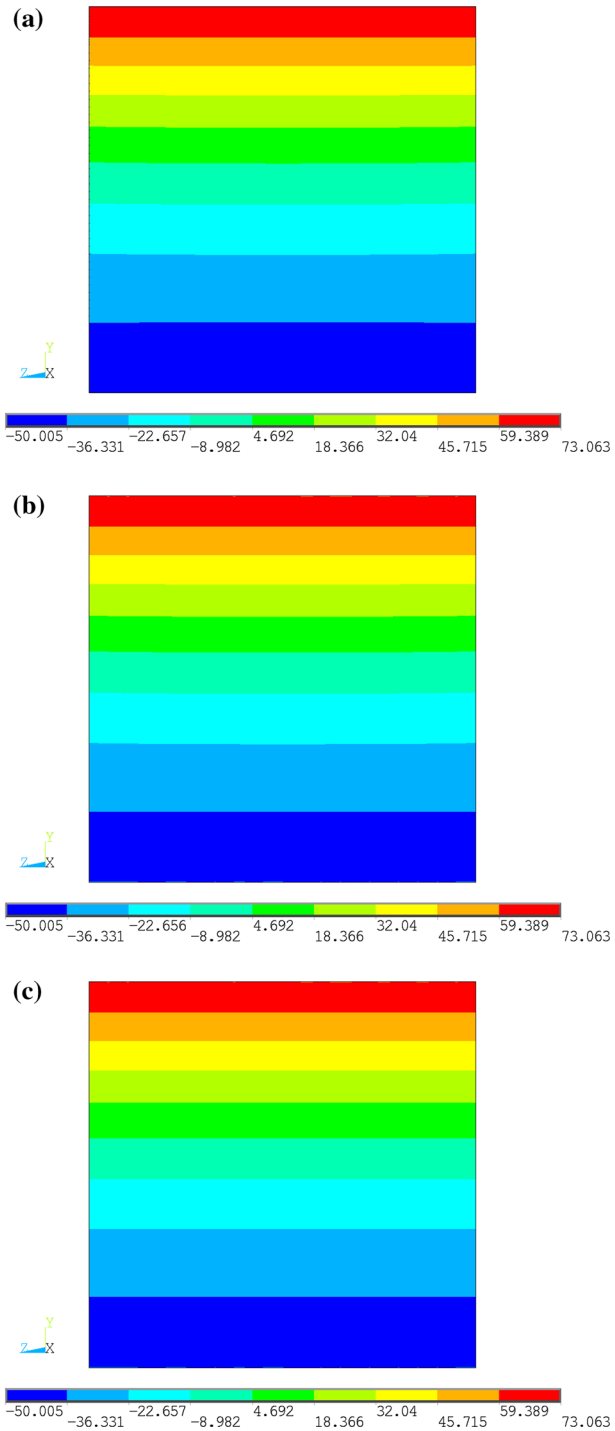

Fig. 9 Dimensionless axial stress $\overline{\sigma}_{xx}$ over the cross-section at $x = l/2$ in a sandwich beam via **a** FEM 3D^a, **b** $N = 9$ and **c** TBT, $n_y = 1$

$$c_{\mathrm{F}} = \frac{2}{\sqrt{N_n}} \tag{49}$$

for data fitting and the solution of nonlinear partial differential equations over a constant unit square domain. In this work, the cross-section dimensions are fixed, and the length-to-side parameter is varied by changing the beam length l. This calls for the length of the beam to explicitly appear in the shape parameter:

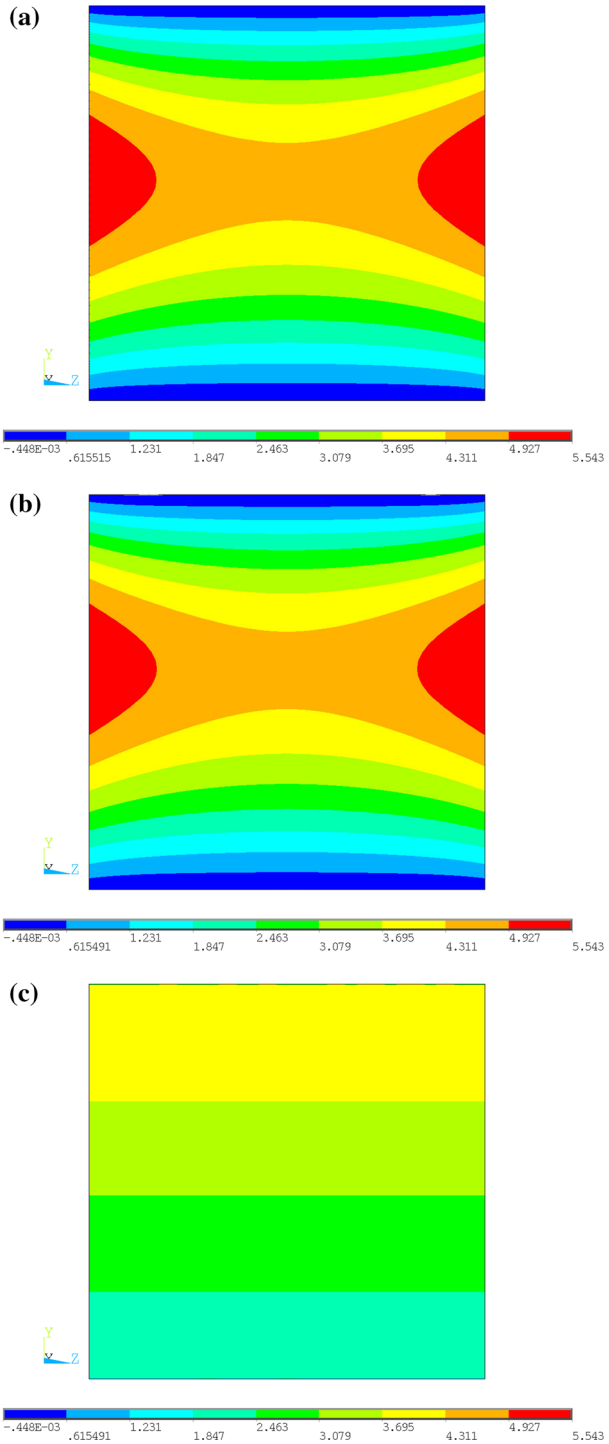

Fig. 10 Dimensionless shear stress $\overline{\sigma}_{xy}$ over the cross-section at $x = 0$ in a sandwich beam via **a** FEM 3D^a, **b** $N = 9$ and **c** TBT, $n_y = 1$

$$c_{\mathrm{P}} = \frac{2}{\sqrt{N_n}} l. \tag{50}$$

A shape parameter as low as $c_{\mathrm{F}}/2$ and as high as $2c_{\mathrm{P}}$ is considered. The number of nodes N_n is equal to 21. The material gradation exponent n_y is equal to one. Both slender and deep beams are considered. A

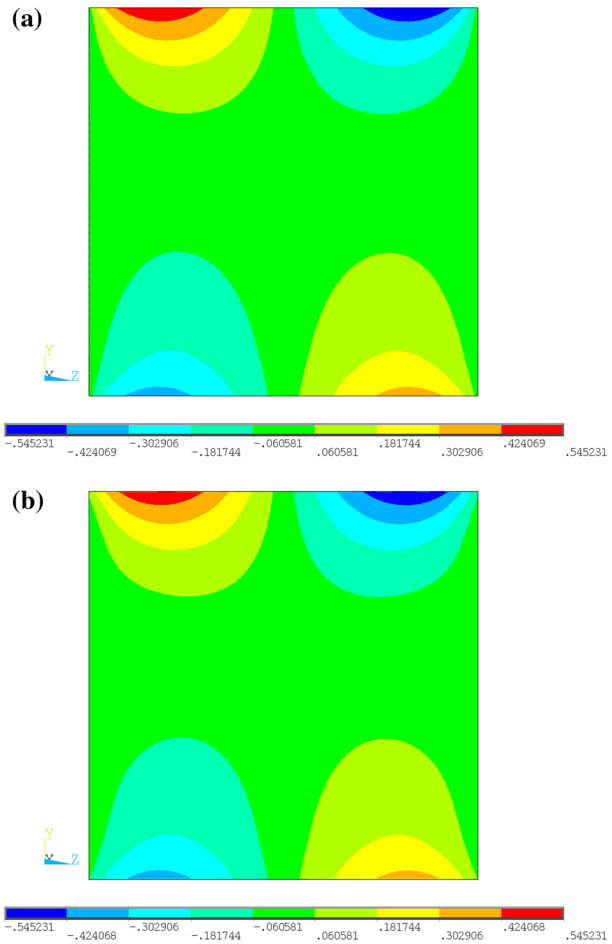

Fig. 11 Dimensionless shear stress $\overline{\sigma}_{xz}$ over the cross-section at $x = 0$ in a sandwich beam via **a** FEM 3D[a] and **b** $N = 9,\ n_y = 1$

second-order beam theory is considered. Higher-order models yield similar results, and they are not presented for the sake of brevity.

Figure 3 shows the normalised difference between the RBF solution and the corresponding Navier-type one in the case of the transverse displacement u_y, the normal stress σ_{xx} and the shear one σ_{xy}:

$$e_{u_y} = \left| \frac{u_{y\text{RBF}} - u_{y\text{Navier}}}{u_{y\text{Navier}}} \right|, \quad e_{\sigma_{xx}} = \left| \frac{\sigma_{xx\text{RBF}} - \sigma_{xx\text{Navier}}}{\sigma_{xx\text{Navier}}} \right|, \quad e_{\sigma_{xy}} = \left| \frac{\sigma_{xy\text{RBF}} - \sigma_{xy\text{Navier}}}{\sigma_{xy\text{Navier}}} \right|. \tag{51}$$

For small values of the shape parameter, the errors are high. For the considered cases, a shape parameter that does not explicitly account for the beam length yields inaccurate results for both slender and deep beams, whereas results computed for $c = c_{\text{P}}$ are accurate. This is believed to be due to the fact that a parameter representative of the leading dimension of the structure should be explicitly considered. A more regular convergence is observed in the case of deep beams than for slender ones. In the remaining of the paper, a shape parameter equal to c_{P} is used.

6.1.2 Influence of the number of nodes

The convergence of the normalised difference between the RBF solution and the corresponding Navier-type in Eq. (51) versus the number of nodes is shown in Figs. 4 and 5. The transverse displacement u_y, the normal stress σ_{xx} and the shear one σ_{xy} are considered. Both uniform and Chebyshev node distributions are used. The number of nodes ranges from 5 up to 31. Chebyshev's node distribution presents a faster convergence when compared with the uniform one. As shown in Fasshauer [58], the rate of convergence is not constant. In the case of short beams, results converge faster than for long beams. For $N_n = 21$, the percentage normalised difference is about 0.6, at worst.

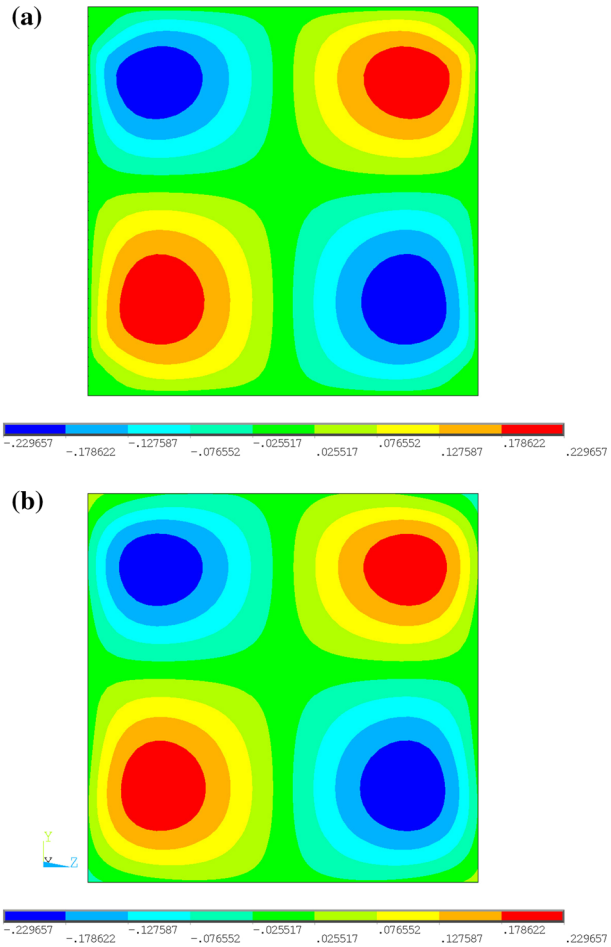

Fig. 12 Dimensionless shear stress $\overline{\sigma}_{yz}$ over the cross-section at $x = l/2$ in a sandwich beam via **a** FEM 3D[a] and **b** $N = 9,\ n_y = 1$

6.1.3 Influence of the expansion order

The dimensionless displacements are reported in Tables 2 and 3 for several expansion orders in the case of $l/a = 100$ and 10, respectively. For slender beams, TBT yields accurate results. In the case of thick beams, a second-order theory overestimates $\overline{u}_z$ by about 4 % with respect to the reference solution. A ninth-order solution matches the refined reference FEM three-dimensional solution. The dimensionless normal and shear stresses $\overline{\sigma}_{xx}$ and $\overline{\sigma}_{xy}$ are presented in Tables 4 and 5. The shear stress $\overline{\sigma}_{xy}$ is not accurately predicted via a second-order theory or TBT as also shown by its variation along the y-axis at $x = 0$ and $z = b/2$ presented in Fig. 6. A thick beam and $n_y = 0.5$ are considered. Results obtained by a third-order theory are accurate but in the neighbourhood of cross-section top and bottom where the stress-free boundary condition is not satisfied. A fifth-order theory matches the FEM reference solution. Figure 7 shows the variation of the transverse normal stress $\overline{\sigma}_{yy}$ along the y-axis at $x = l/2$ and $z = b/2$ for $n_y = 1$. Results obtained by a ninth-order theory match the reference FEM three-dimensional solution, whereas in the case of a fifth-order theory, top and bottom stress boundary conditions are not satisfied. A second-order theory does not yield accurate results.

6.2 Sandwich beams

A sandwich FGM beam, as shown in Fig. 8, is considered. The bottom face is made of steel, whereas the top face is made of alumina. They have equal thickness $h_f = a/10$. The core, whose thickness is h_c, is made of an alumina–steel FGM, fully metallic at $y = h_f$ and fully ceramic at $y = a - h_f$. Dimensionless displacements and stresses are reported in Tables 6 and 7, respectively. For the sake of brevity, only thick

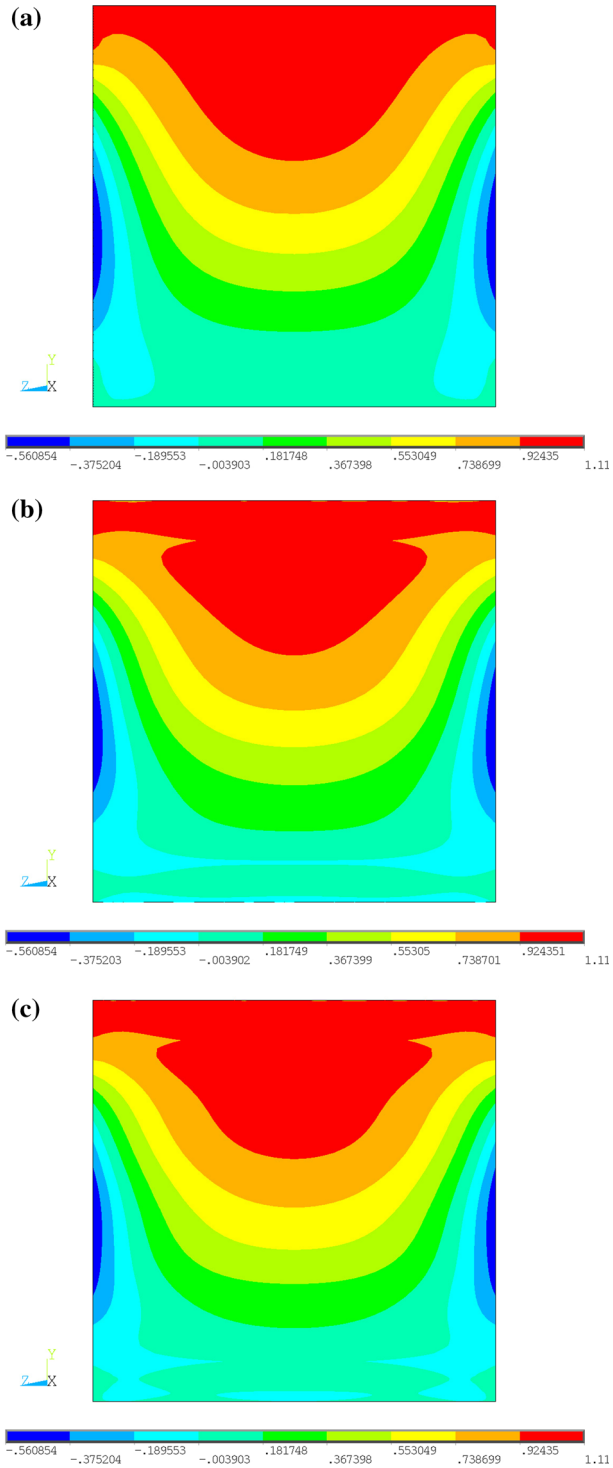

Fig. 13 Dimensionless normal stress $\overline{\sigma}_{yy}$ over the cross-section at $x = l/2$ in a sandwich beam via **a** FEM 3D^a, **b** $N = 9$ and **c** $N = 12$, $n_y = 1$

beams are investigated. Results are similar to those of the mono-layer beam. TBT yields good results for the transverse displacement $\overline{u}_y$ and the normal stress $\overline{\sigma}_{xx}$. This is also confirmed by Fig. 9 where the variation of $\overline{\sigma}_{xx}$ over the cross-section at $x = l/2$ is qualitatively presented as a colour map. The solutions obtained via the FEM 3D^a model, a ninth-order model and TBT are compared. As far as the shear stress component $\overline{\sigma}_{xy}$

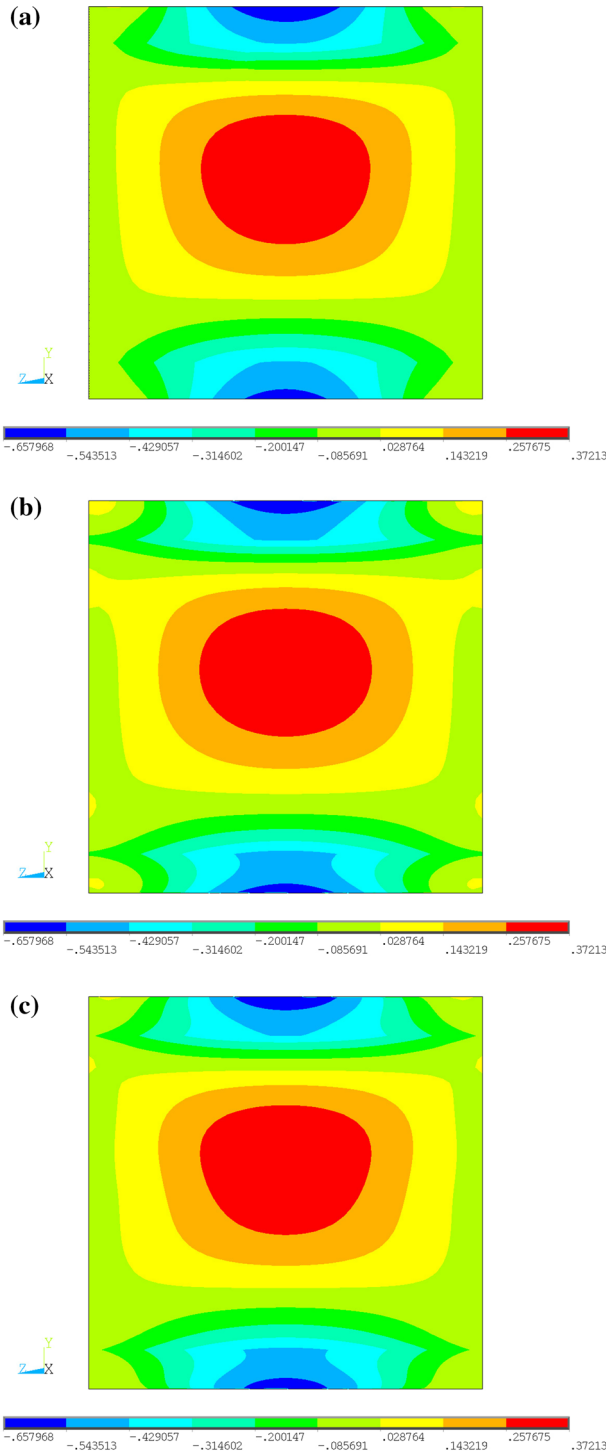

Fig. 14 Dimensionless normal stress $\overline{\sigma}_{zz}$ over the cross-section at $x = l/2$ in a sandwich beam via **a** FEM 3D[a], **b** $N = 9$ and **c** $N = 12$, $n_y = 1$

is concerned, higher-order models are required to obtain an accurate solution as also shown in Fig. 10. The colour maps of the shear stresses $\overline{\sigma}_{xz}$ and $\overline{\sigma}_{yz}$ are presented in Figs. 11 and 12, respectively. A ninth-order theory matches the reference three-dimensional FEM solution. Figures 13 and 14 show the normal stresses $\overline{\sigma}_{yy}$ and $\overline{\sigma}_{zz}$. A twelfth-order theory is also considered. The considered theories compare fairly well with the

reference solution. For instance, the maximum value of $\overline{\sigma}_{yy}$ is 1.110 for $N = 9$, 1.076 for $N = 12$ and 1.027 in the case of FEM 3D^a. The main differences are observed in correspondence with the FGM layer interfaces. Besides the assumption of an higher approximation order, a possible enhancement of the proposed models could consist in the use of a mixed approach where both displacements and stresses are considered as primary unknowns.

7 Conclusions

A unified formulation of one-dimensional beam models has been proposed for the static analysis of functionally graded beams. Higher-order models that account for non-classical effects such as shear deformations and in- and out-of-plane warping can be formulated straightforwardly. Timoshenko's classical model is regarded as a particular case. As a first endeavour, a meshless method based on multiquadric radial basis functions has been adopted. Mono-layer and sandwich beams have been investigated. Results have been validated by comparison with analytical Navier-type solutions and three-dimensional FEM solutions obtained via the commercial code ANSYS. The numerical investigations point out that the choice of the radial basis function shape parameter has an important influence on the accuracy of the solution. A shape parameter that explicitly scales with the length of the beam has been used. The presented results show that three-dimensional displacement and stress components can be computed accurately as long as an appropriate approximation order is used.

References

1. Koizumi, M.: FGM activities in Japan. Compos. Part B Eng. **28**, 1–4 (1997)
2. Suresh, S., Mortensen, A.: Fundamentals of Functional Graded Materials. IOM Communications Limited, London (1998)
3. Miyamoto, Y., Kaysser, W.A., Rabin, B.H., Kawasaki, A., Ford, R.G.: Functionally Graded Materials: Design, Processing and Applications. Kluwer Academic, Boston, MA (1999)
4. Watanabe, R., Nishida, T., Hirai, T.: Present status of research on design and processing of functionally graded materials. Met. Mater. Int. **9**, 513–519 (2003)
5. Birman, V., Byrd, L.W.: Modeling and analysis of functionally graded materials and structures. Appl. Mech. Rev. **60**, 195–216 (2007)
6. Sankar, B.V.: An elasticity solution for functionally graded beams. Compos. Sci. Technol. **61**, 689–696 (2001)
7. Chakraborty, A., Gopalakrishnan, S., Reddy, J.N.: A new beam finite element for the analysis of functionally graded materials. Int. J. Mech. Sci. **45**, 519–539 (2003)
8. Li, X.F.: A unified approach for analyzing static and dynamic behaviors of functionally graded Timoshenko and Euler–Bernoulli beams. J. Sound Vib. **318**, 1210–1229 (2008)
9. Kapuria, S., Bhattacharyya, M., Kumarb, A.N.: Bending and free vibration response of layered functionally graded beams: a theoretical model and its experimental validation. Compos. Struct. **82**, 390–402 (2008)
10. Bîrsan, M., Altenbach, H., Sadowski, T., Eremeyev, V.A., Pietras, D.: Deformation analysis of functionally graded beams by the direct approach. Compos. Part B Eng. **43**, 1315–1328 (2012)
11. Zhilin, P.A.: Mechanics of deformable directed surfaces. Int. J. Solids Struct. **12**, 635–648 (1976)
12. Murin, J., Aminbaghai, M., Hrabovskỳ, J., Kutiš, V., Kugler, S.: Modal analysis of the FGM beams with effect of the shear correction function. Compos. Part B Eng. **45**, 1575–1582 (2013)
13. Kugler, St., Fotiu, P.A., Murin, J.: The numerical analysis of FGM shells with enhanced finite elements. Eng. Struct. **49**, 920–935 (2013)
14. Kutiš, V., Murin, J., Belák, R., Paulech, J.: Beam element with spatial variation of material properties for multiphysics analysis of functionally graded materials. Comput. Struct. **89**, 1192–1205 (2011)
15. Liu, G.R., Gu, Y.T.: An Introduction to Meshfree Methods and Their Programming. Springer, Berlin (2005)
16. Liu, G.R.: Meshfree Methods: Moving Beyond the Finite Element Method. CRC Press Inc, Boca Raton, FL (2009)
17. Hardy, R.L.: Multiquadric equations of topography and other irregular surfaces. J. Geophys. Res. **76**, 1905–1915 (1971)
18. Kansa, E.J.: Multiquadrics—a scattered data approximation scheme with applications to computational fluid-dynamics—I. Surface approximations and partial derivative estimates. Comput. Math. Appl. **19**, 127–145 (1990)
19. Kansa, E.J.: Multiquadrics—a scattered data approximation scheme with applications to computational fluid-dynamics—II. Solutions to parabolic, hyperbolic and elliptic partial differential equations. Comput. Math. Appl. **19**, 147–161 (1990)
20. Wu, Z.M.: Hermite–Bikhoff interpolation of scattered data by radial basis function. Approx. Theory Appl. **8**, 1–10 (1992)
21. Wu, Z.M.: Advances in Computational Mathematics, volume 202 of Lecture Notes on Pure and Applied Mathematics. chapter Solving PDE with Radial Basis Function and the Error Estimation, GuangZhou (1998)
22. Liu, G.R., Gu, Y.T.: A local radial point interpolation method (LRPIM) for free vibration analyses of 2-D solids. J. Sound Vib. **246**, 29–46 (2001)
23. Liu, G.R., Wang, J.G.: A point interpolation meshless method based on radial basis functions. Int. J. Numer. Method Eng. **54**, 1623–1648 (2002)
24. Ferreira, A.J.M.: A formulation of the multiquadric radial basis function method for the analysis of laminated composite plates. Compos. Struct. **59**, 385–392 (2003)
25. Ferreira, A.J.M.: Thick composite beam analysis using a global meshless approximation based on radial basis functions. Mech. Adv. Mater. Struct. **10**, 271–284 (2003)

26. Roque, C.M.C., Ferreira, A.J.M., Neves, A.M.A., Fasshauer, G.E., Soares, C.M.M., Jorge, R.M.N.: Dynamic analysis of functionally graded plates and shells by radial basis functions. Mech. Adv. Mater. Struct. **17**, 636–652 (2010)
27. Neves, A.M.A., Ferreira, A.J.M., Carrera, E., Roque, C.M.C., Cinefra, M., Jorge, R.M.N., Soares, C.M.M.: Bending of FGM plates by a sinusoidal plate formulation and collocation with radial basis functions. Mech. Res. Commun. **38**, 368–371 (2011)
28. Neves, A.M.A., Ferreira, A.J.M., Carrera, E., Roque, C.M.C., Cinefra, M., Jorge, R.M.N., Soares, C.M.M.: A quasi-3D sinusoidal shear deformation theory for the static and free vibration analysis of functionally graded plates. Compos. Part B Eng. **43**, 711–725 (2012)
29. Neves, A.M.A., Ferreira, A.J.M., Carrera, E., Cinefra, M., Roque, C.M.C., Jorge, R.M.N., Soares, C.M.M.: A quasi-3D hyperbolic shear deformation theory for the static and free vibration analysis of functionally graded plates. Compos. Struct. **94**, 1814–1825 (2012)
30. Neves, A.M.A., Ferreira, A.J.M., Carrera, E., Cinefra, M., Roque, C.M.C., Jorge, R.M.N., Soares, C.M.M.: Static, free vibration and buckling analysis of isotropic and sandwich functionally graded plates using a quasi-3D higher-order shear deformation theory and a meshless technique. Compos. Part B Eng. **44**, 657–674 (2013)
31. Neves, A.M.A., Ferreira, A.J.M., Carrera, E., Cinefra, M., Roque, C.M.C., Jorge, R.M.N., Soares, C.M.M.: Free vibration analysis of functionally graded shells by a higher-order shear deformation theory and radial basis functions collocation, accounting for through-the-thickness deformations. Eur. J. Mech. A Solids **37**, 24–34 (2013)
32. Davydov, O., Oanh, D.T.: Adaptive meshless centres and RBF stencils for Poisson equation. J. Comput. Phys. **230**, 287–304 (2011)
33. Carrera, E.: Theories and finite elements for multilayered plates and shells: a unified compact formulation with numerical assessment and benchmarking. Arch. Comput. Methods Eng. **10**, 215–296 (2003)
34. Carrera, E., Giunta, G.: Hierarchical models for failure analysis of plates bent by distributed and localized transverse loadings. J. Zhejiang Univ. Sci. A **9**, 600–613 (2008)
35. Carrera, E., Giunta, G.: Hierarchical evaluation of failure parameters in composite plates. AIAA J. **47**, 692–702 (2009)
36. Carrera, E., Giunta, G.: Exact, hierarchical solutions for localised loadings in isotropic, laminated and sandwich shells. J. Press. Vessel Technol. **131**, 041202 (2009)
37. Carrera, E., Giunta, G.: Refined beam theories based on a unified formulation. Int. J. Appl. Mech. **2**, 117–143 (2010)
38. Carrera, E., Giunta, G., Nali, P., Petrolo, M.: Refined beam elements with arbitrary cross-section geometries. Comput. Struct. **88**, 283–293 (2010)
39. Carrera, E., Giunta, G., Petrolo, M.: Beam Structures: Classical and Advanced Theories. Wiley-Blackwell, New York (2011)
40. Giunta, G., Belouettar, S., Carrera, E.: Analysis of FGM beams by means of classical and advanced theories. Mech. Adv. Mater. Struct. **17**, 622–635 (2010)
41. Giunta, G., Biscani, F., Belouettar, S., Carrera, E.: Analysis of thin-walled beams via a one-dimensional unified formulation. Int. J. Appl. Mech. **3**, 407–434 (2011)
42. Giunta, G., Biscani, F., Belouettar, S., Ferreira, A.J.M., Carrera, E.: Free vibration analysis of composite beams via refined theories. Compos. Part B Eng. **44**, 540–552 (2013)
43. Giunta, G., Metla, N., Koutsawa, Y., Belouettar, S.: Free vibration and stability analysis of three-dimensional sandwich beams via hierarchical models. Compos. Part B Eng. **47**, 326–338 (2013)
44. Giunta, G., Crisafulli, D., Belouettar, S., Carrera, E.: A thermo-mechanical analysis of functionally graded beams via hierarchical modelling. Compos. Struct. **95**, 676–690 (2013)
45. Giunta, G., Koutsawa, Y., Belouettar, S., Hu, H.: Static, free vibration and stability analysis of three-dimensional nano-beams by atomistic refined models accounting for surface free energy effect. Int. J. Solids Struct. **50**, 1460–1472 (2013)
46. Philips, G.M.: Interpolation and Approximation by Polynomials. Springer, Berlin (2003)
47. Praveen, G.N., Reddy, J.N.: Nonlinear transient thermoelastic analysis of functionally graded ceramic-metal plates. Int. J. Solids Struct. **35**, 4457–4476 (1998)
48. Carrera, E., Brischetto, S.: Analysis of thickness locking in classical, refined and mixed multilayered plate theories. Compos. Struct. **82**, 549–562 (2008)
49. Carrera, E., Brischetto, S.: Analysis of thickness locking in classical, refined and mixed theories for layered shells. Compos. Struct. **85**, 83–90 (2008)
50. Cowper, G.R.: The shear co-efficient in Timoshenko beam theory. J. Appl. Mech. **33**, 335–340 (1996)
51. Murty, A.V.K.: Analysis of short beams. AIAA J. **8**, 2098–2100 (1970)
52. Carrera, E., Petrolo, M.: On the effectiveness of higher-order terms in refined beam theories. J. Appl. Mech. **78**, 021013–102101317 (2011)
53. Roque, C.M.C., Ferreira, A.J.M.: Numerical experiments on optimal shape parameters for radial basis functions. Numer. Methods Partial Differ. Eq. **26**, 675689 (2010)
54. Hon, Y.C., Schaback, R.: On unsymmetric collocation by radial basis functions. Appl. Math. Comput. **119**, 177–186 (2001)
55. Kansa, E.J., Hon, Y.C.: Circumventing the ill-conditioning problem with multiquadric radial basis functions: applications to elliptic partial differential equations. Comput. Math. Appl. **39**, 123–137 (2000)
56. ANSYS v10.0 theory manual. ANSYS Inc., Southpointe, PA (2006)
57. Press, W.H., Teukolsky, S.A., Vetterling, W.T., Flannery, B.P.: Numerical Recipes: The Art of Scientific Computing. 3rd edn. Cambridge University Press, New York (2007)
58. Fasshauer, G.E.: Newton iteration with multiquadrics for the solution of nonlinear PDEs. Comput. Math. Appl. **43**, 423–438 (2002)